

Biological imaging of chemical bonds by stimulated Raman scattering microscopy

Fanghao Hu^{1,3}, Lixue Shi^{1,3} and Wei Min^{1,2*}

All molecules consist of chemical bonds, and much can be learned from mapping the spatiotemporal dynamics of these bonds. Since its invention a decade ago, stimulated Raman scattering (SRS) microscopy has become a powerful modality for imaging chemical bonds with high sensitivity, resolution, speed and specificity. We introduce the fundamentals of SRS microscopy and review innovations in SRS microscopes and imaging probes. We highlight examples of exciting biological applications, and share our vision for potential future breakthroughs for this technology.

Chemical bonds are the basic units of molecules. Dictated by quantum mechanics, the vibrations of chemical bonds occur at discrete frequencies depending on the specific type and local environment of the chemical bonds. As such, they provide intrinsic and chemically informative contrasts for molecular science, and are the very foundation of vibrational spectroscopy and microscopy. As one of the most powerful and fast-evolving vibrational imaging techniques, stimulated Raman scattering (SRS) microscopy can map distribution of chemical bonds in three-dimensional space and real time. SRS as a contrast mechanism for microscopy was first demonstrated on polystyrene beads with a femtosecond amplifier laser source and a photodiode array, in 2007¹. SRS bio-imaging was achieved in 2008 by using a high-repetition-rate picosecond laser source and a high-frequency modulation transfer detection scheme² to achieve much higher sensitivity and speed, alongside the low photo-damage needed for biological systems. This work was accompanied by two other reports, in 2009, describing similar applications to biological systems^{3,4}.

As a nonlinear optical process, SRS uses two synchronized pulsed lasers, one known as the pump beam and the other as the Stokes beam, to coherently excite the selected molecular vibration. When the frequency difference between the pump and the Stokes lasers matches the vibration (ω_v) of the chemical bond of interest, vibrational activation rates can be drastically amplified through quantum stimulation of photons in the Stokes beam, on top of the inherently weak spontaneous Raman scattering (Fig. 1a). Quantum mechanically, this stimulated scattering effect is analogous to stimulated emission⁵ and has been used in many spectroscopic studies^{6–9}. In SRS microscopy (Fig. 1b), both laser beams are spatially and temporally overlapped, and focused collinearly into a diffraction-limit spot inside the sample. The stimulation factor can go up to 10^8 at the tight microscope focus¹⁰, which confers high sensitivity and speed of SRS bio-imaging.

The detection scheme of SRS is unique and different from most other optical microscopy methods. By virtue of energy conservation, each vibrational excitation event is accompanied by one photon loss in the pump beam (stimulated Raman loss, SRL) and one photon gain in the Stokes beam (stimulated Raman gain, SRG), respectively. Hence, SRS signal is detected as a relative intensity change of the incident laser ($\Delta I/I \sim 10^{-3} - 10^{-7}$, Fig. 1c). To achieve sensitive detection above the low-frequency laser background noise,

a high-frequency (megahertz) modulation is applied to one laser beam and the modulation transfer to the other beam is measured to extract SRS signal using a radio-frequency (RF) lock-in amplifier (Fig. 1c). This removes the noise from the slow laser intensity fluctuation and achieves near shot-noise-limited sensitivity (Fig. 1d). With the SRS signal being registered at each pixel, three-dimensional images can be readily acquired by raster-scanning the laser focus across the samples using a laser-scanning microscope in either transmitted or reflected light directions.

SRS microscopy has emerged as one of the most promising techniques for imaging chemical bonds for biomedicine^{11–13}. Compared to the conventional spontaneous Raman microscopy, SRS offers more than 1,000-times faster imaging speed and is free from sample autofluorescence interference¹⁰. Different from another nonlinear Raman technique called coherent anti-Stokes Raman scattering (CARS), SRS offers background-free chemical contrast, strict linear concentration dependence, and authentic Raman spectra by virtue of direct detection of energy exchange between chemical bonds and laser fields, facilitating quantitative and straightforward image analysis. In addition, SRS is compatible with confocal and two-photon excited fluorescence microscopy, as well as other nonlinear imaging techniques, such as second harmonic generation, to achieve multi-modal optical imaging. The last ten years have witnessed the blossoming of SRS microscopy, where advances in both optical instruments and imaging probes have found broad applications in life sciences. For the remainder of this Perspective, we focus on reviewing the major innovations in SRS microscopy.

Instrument development

Complex biological systems constantly demand higher speed, sensitivity and spatial resolution of imaging techniques, to capture the fast spatiotemporal dynamics. For this purpose, thanks to the numerous efforts devoted to developing physical instruments, SRS microscopy has achieved fast imaging speed up to video rate, rapid multi-mode excitation, detection sensitivity down to single molecules, and spatial resolution with potential of breaking the diffraction limit, as well as volumetric tissue and in vivo animal and human imaging.

Imaging speed. With strong amplification through stimulated emission, SRS can achieve imaging speeds comparable to those of

¹Department of Chemistry, Columbia University, New York, NY, USA. ²Kavli Institute for Brain Science, Columbia University, New York, NY, USA.

³These authors contributed equally: Fanghao Hu, Lixue Shi. *e-mail: wm2256@columbia.edu

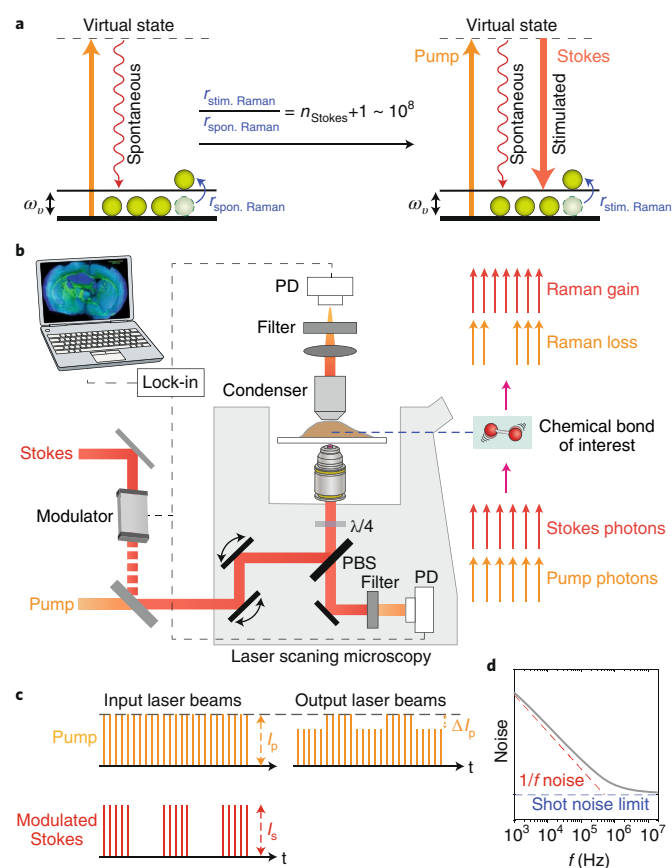


Fig. 1 | Principle of SRS microscopy. **a**, Energy-level diagrams of spontaneous (spon.) Raman scattering and SRS. In SRS, highly efficient vibrational excitation can occur as a result of the stimulated (stim.) emission by introducing an intense Stokes beam. Vibrational transition rates can be enhanced by a factor of $n_{\text{Stokes}} + 1$ (n_{Stokes} is the number of photons in a mode of the Stokes beam, which is $\sim 10^8$). **b**, SRS microscope setup. Pump and Stokes laser beams are combined and focused into the sample. SRS signal (SRL or SRG) can be detected in either transmitted or reflected directions. PD, photodiode; PBS, polarizing beamsplitter. **c**, SRS detection scheme using high-frequency modulation/demodulation. Temporal profiles of the input and output pump and Stokes pulse trains. **d**, High-frequency modulation (> 1 MHz) can suppress low-frequency laser intensity fluctuation noise to approach the shot-noise limit.

confocal fluorescence microscopy. The typical acquisition time for SRS is 0.1–10 seconds per frame, with pixel dwell time in 1–100 μs , depending on the signal size. Using a fast lock-in amplifier and a resonant galvanometer mirror, video-rate SRS imaging has been achieved with 25–110 frames s^{-1} (refs. 14–16). These open up broad applications for live-cell biology.

Multi-mode excitation schemes. Raman scattering is inherently a broadband process that contains the entire vibrational spectrum of the sample with rich chemical information. Single-mode SRS excitation using two narrowband picosecond (ps) lasers has been commonly used for imaging samples with known components and well-resolved Raman frequencies. To retrieve the full chemical information, multi-mode excitations across a broad range of Raman spectrum are needed. Several commercial laser sources are available for SRS microscopy, including picoEmerald picosecond laser from Applied Physics & Electronics, Inc. (<http://www.ape-america.com/products/opa-opo-harmonixx/opo-mhz-ghz/pico-emerald-s>) and InSight X3 femtosecond laser from Spectra-Physics

(<https://www.spectra-physics.com/products/ultrafast-lasers/insight-x3>). Invenio Imaging Inc. has produced a commercial SRS system for tissue histology based on a fiber laser¹⁷, and Leica recently introduced the first fully integrated SRS research microscope (<https://www.leica-microsystems.com/products/confocal-microscopes/p/leica-tcs-sp8-cars/>). Depending on the available laser source, different excitation and detection schemes have been developed for SRS microscopy, including the sequential wavelength tuning scheme, and parallel multi-mode excitation and detection scheme.

Several methods are available to achieve sequential wavelength tuning. With two synchronized picosecond lasers, multi-mode SRS imaging can be readily achieved at high spectral resolution by wavelength sweeping (Fig. 2a), through temperature control of nonlinear crystal with large tuning range, or by using an electro-optical tuneable Lyot filter for fast tuning over a small range^{18,19}. A broadband femtosecond (fs) laser source can also be used to achieve high-speed multi-mode excitation. Pulse shaping techniques have been developed to rapidly select narrowband frequency using spectral filters^{20,21}. Based on a customized laser system, an impressively fast imaging rate of 30 frames s^{-1} has been achieved¹⁵, covering a wide spectral window of ~ 300 cm^{-1} with fine spectral resolution at ~ 4 cm^{-1} . Among the sequential wavelength tuning schemes, the spectral-focusing method is gaining popularity (Fig. 2b) by linearly chirping two broadband laser pulses and then scanning the time delays^{22–25}. Using a resonant mirror to rapidly adjust the time delay, a 200- cm^{-1} SRS spectrum with ~ 30 cm^{-1} spectral resolution can be acquired in 83 μs (ref. 26). A larger spectral coverage of 650 cm^{-1} with higher spectral resolution (~ 10 cm^{-1}) is achievable based on parabolic fiber amplification, albeit at a slower speed of ~ 1 ms per spectrum²⁷. On the same spectral-focusing platform, simultaneous two-color imaging has also been demonstrated at 8 frames s^{-1} , by using engineered pulse profile and dual-phase lock-in detection²⁸.

Parallel SRS imaging over a large spectral window can be achieved by using a combination of ps and fs lasers for broadband excitation (Fig. 2c). Multi-channel array detections and lock-in demodulations are often required to simultaneously detect the broadband signal^{29,30}. A fast complementary metal oxide semiconductor (CMOS) array detector synchronized to the modulation frequency can be also applied³¹. Moreover, a 16-channel tuned amplifier array was built to extract SRS signals in a lock-in-free manner, which can acquire an SRS spectrum of ~ 200 cm^{-1} in 32 μs (ref. 32) and was reduced to 5 μs with 32 channels³³. Further, if an array detector is not applicable, a single detector with lock-in amplifier can be used to extract the multi-mode SRS signals through fast Fourier transform³⁴, when the excitation wavelengths in the broadband pulse are modulated at different radiofrequencies. High-speed SRS imaging across a ~ 200 cm^{-1} window with ~ 15 cm^{-1} spectral resolution has been achieved at 60 μs per spectrum³⁵. Lastly, photonic time stretch technique can be applied to measure broadband SRS signal with a single detector³⁶, which covers a window of ~ 500 cm^{-1} in 400 μs with spectral resolution of 10 cm^{-1} .

Excitation spectroscopy and detection sensitivity. SRS imaging typically has sensitivity in the μM – mM range for most chemical bonds. Due to the use of high-frequency modulation transfer and a lock-in detection scheme, SRS is free from laser fluctuation noise and the detection sensitivity scales linearly with the square root of the acquisition time¹⁰. Typically for bio-imaging, the detection sensitivity of $\Delta I/I$ approaches $\sim 10^{-7}$ at 100- μs acquisition time. This corresponds to several mM of typical C=C double bonds and $\sim 10^5$ molecules in the focal volume (~ 0.1 femtoliter). To further boost the sensitivity, a series of special vibrational probes can be used, including alkyne, diyne and polyynes^{37,38}, which achieved sensitive detection down to μM and are reviewed in detail in the next section.

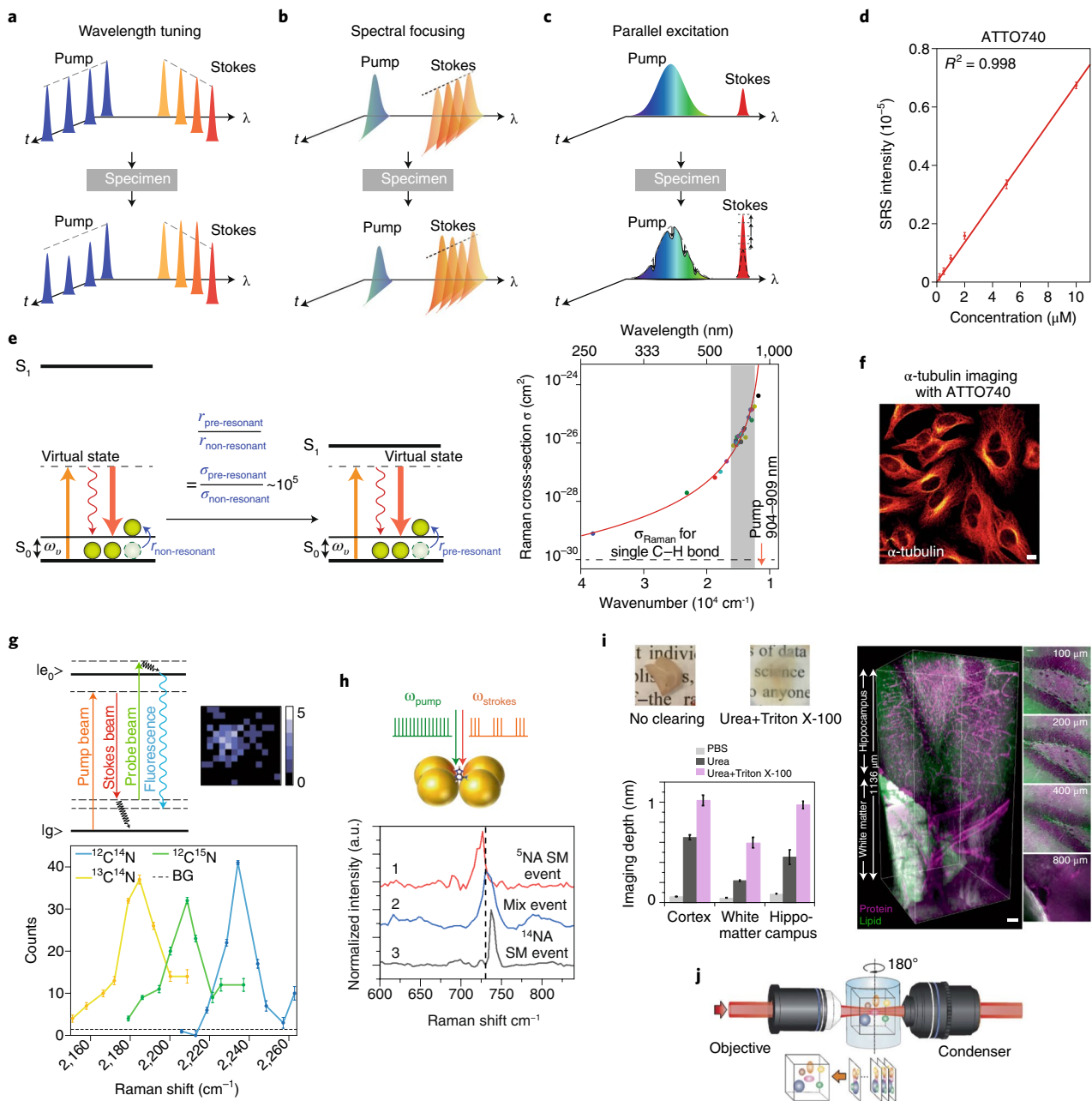


Fig. 2 | Instrumental advances. Multi-mode excitation schemes. **a**, Wavelength tuning of picosecond pump and Stokes with sequential detection of SRG. **b**, Delay time tuning of chirped femtosecond pump and Stokes with sequential detection of SRG. **c**, Parallel broadband excitation with fs pump and ps Stokes for simultaneous detection of SRL. **d**, Detection limit of epr-SRS can be pushed to 250 nM with 1-ms time constant. **e**, Energy diagram for non-resonant and electronic pre-resonant SRS (left). Up to 10^5 enhancements can be obtained for the vibrational transition rate. Raman cross-section increases under electronic pre-resonant excitation with the approaching of electronic transition (right). **f**, epr-SRS imaging of ATTO740 immuno-labelled α -tubulin. Scale bar, 10 μm . **g**, Stimulated Raman excited fluorescence (SREF) achieves all-far-field single molecule vibrational imaging. Energy diagram of SREF and representative single-molecule image of rhodamine 800 (Rh800; upper). Single-molecule Raman spectrum for Rh800 isotopologues (lower). **h**, Plasmon-enhanced SRS (PESRS) to reach single-molecule sensitivity. Schematic illustration of plasmonic enhancement of adenine on gold nanostructure (upper). Single-pixel PESRS spectra showing a pure ^{15}N -adenine (^{14}NA) single molecule (SM) event (1), a mix event (2) and a pure ^{14}N -adenine single molecule event (lower). **i**, Volumetric SRS imaging based on a Raman-tailored tissue-clearing method. Imaging depth can be improved by tenfold with urea and Triton treatment (left). Volumetric reconstruction of the hippocampus and white matter (right). Scale bar, 50 μm . **j**, Stimulated Raman projection and tomography based on Bessel beam for high-speed volumetric chemical imaging.

SRS detection sensitivity closely depends on the corresponding excitation spectroscopy, which can be drastically enhanced by coupling to electronic resonance or localized surface plasmon. While most SRS imaging does not involve chromophores, electronic pre-resonance SRS (epr-SRS) has been developed for light-absorbing

chromophores to push the detection limit to sub- μM (~ 50 molecules in the focal volume) with 1 ms acquisition time (Fig. 2d), while maintaining the sharp vibrational feature with high chemical selectivity³⁹. By carefully tuning the molecular absorptions of chromophores close to, but not identical to, SRS excitation wavelength,

epr-SRS can drastically improve the Raman scattering cross-section by up to 10^5 times (Fig. 2e). For the first time, protein-specific immuno-imaging of α -tubulin was demonstrated with high vibrational contrast by epr-SRS (Fig. 2f).

Built on epr-SRS excitation of fluorescent dyes, even higher sensitivity can be achieved by stimulated Raman-excited fluorescence (SREF) microscopy⁴⁰ (Fig. 2g). Through up-converting the epr-SRS-excited vibrational population to electronic excited state for the subsequent background-free fluorescence detection, this technique combines the fine chemical specificity of vibrational transition with the superb molecular sensitivity of fluorescence. This is the first time that Raman spectroscopy and imaging are achieved at the ultimate single-molecule level without any plasmonic enhancement.

Near-field plasmonic enhancement is also applied to enhance nonlinear Raman signal⁴¹, which was first achieved in time-resolved CARS microscopy to visualize the vibrational wave packet motion of a single molecule⁴². With $\sim 10^7$ signal enhancement, single-molecule sensitivity of adenine was recently demonstrated in plasmon-enhanced SRS with a 10- μ s acquisition time⁴³ (Fig. 2h), requiring the use of gold nanostructures and de-noising algorithm.

Spatial resolution. Spatial resolution is another key parameter for subcellular imaging. As a nonlinear imaging technique, SRS has intrinsically optical sectioning capability and reaches the same diffraction-limited resolution as in two-photon excited fluorescence microscopy, due to the quadratic dependence on the intensity. Using near-infrared light for excitation (λ ; ~ 800 – 1064 nm), the typical lateral resolution of SRS microscopy is ~ 300 nm and the axial resolution is 1–2 μ m. The spatial resolution can be improved if a shorter excitation wavelength is applicable. By doubling the frequency of the near-infrared laser to blue wavelength of around 450 nm for SRS excitation, a lateral resolution of ~ 130 nm (which is still diffraction-limited) was demonstrated using a high numerical aperture 1.49 objective⁴⁴.

Achieving super-resolution Raman imaging with rich chemical information is an exciting endeavor. Several super-resolution SRS techniques have been proposed to break the diffraction limit by adding a third laser beam to suppress SRS signal through either saturation/depletion or competing SRS processes^{45–47}, which are inspired by the stimulated emission depletion (STED) fluorescence microscopy⁴⁸. An enhancement factor of ~ 2 in lateral resolution can be obtained by using a doughnut-shaped decoherence beam to achieve nonlinear signal suppression in SRS⁴⁹. If an additional laser beam is not available, saturated SRS microscopy has been demonstrated to reach sub-diffraction resolution of ~ 250 nm, by using virtual sinusoidal modulation to extract the second-harmonic order of the SRS signal⁵⁰.

Volumetric 3D imaging. Three-dimensional volumetric imaging allows comprehensive investigation of structures and dynamics in complex biological systems. With the near-infrared excitation wavelength and confined probe volume, SRS microscopy has 3D sectioning capability and deep imaging depth. The typical imaging depth of SRS is 300–500 μ m in less scattering samples, and < 100 μ m in highly scattering samples such as brain tissues, limited by the scattering loss of excitation power and strong surface background.

To achieve volumetric SRS imaging with much greater depth, urea and low-concentration Triton X-100 can be applied to reduce refractive index mismatch and tissue scattering in a Raman-tailored optical clearing technique⁵¹, which achieved more than tenfold increase in imaging depth (~ 1 mm) in tumor and mouse brain tissues (Fig. 2i). To increase volumetric imaging speed, Bessel beam with extended depth of focus (in millimeters) was also applied to generate stimulated Raman projection (SRP) through a 2D lateral scan of the entire volume⁵², which can be combined with sample rotation and tomography to reconstruct 3D structures

(Fig. 2j) with identical resolution (~ 0.83 μ m) in all directions in tens of seconds.

Apparatus for in vivo imaging. Lastly, in vivo imaging with chemical specificity is valuable in the study of live animal models and clinical settings, which require epi-detection configuration of SRS microscopes by using a quarter-wave plate and polarizing beam-splitter to collect the backward-going photons (Fig. 1b). To enhance the signal collection in the epi-direction, a large-area ring-shaped detector can be placed between the objective and the sample, which collects up to 90% of the signal in the backward direction¹⁴. With the special detector for epi-detected SRS, in vivo imaging with high sensitivity has been demonstrated in living mice and humans¹⁴. Besides, a fiber-delivered hand-held SRS microscope is also applicable to achieve background-free in situ and in vivo chemical imaging of brain tissues and live human skin⁵³. Further miniaturization will be desired.

Imaging probe development

SRS microscopy was originally developed as a label-free imaging technique². By targeting endogenous chemical bonds including O–H, C–H, C=C, C=O, S=O, O–P–O, amide and several ring-breathing modes in the cellular fingerprint and high-frequency regions (Fig. 3a), a variety of species have been successfully imaged by label-free SRS microscopy¹¹. This has produced a great body of research works, such as visualizing total proteins^{54,55}, lipids^{56,57}, DNA⁵⁸, cholesterol^{59,60} and cell walls^{61,62}; in cells, tissues and organisms under both physiological and pathological conditions.

Yet, the development of an imaging modality relies on the combination of physical instruments and imaging probes. Indeed, many exciting advances in fluorescence microscopy are made possible by innovations in imaging probes. In this regard, the popular label-free paradigm has limitations, especially on specificity and sensitivity. To bring chemistry innovations into the field, a variety of vibrational probes have been designed for SRS imaging of biological systems, representing an exciting direction of development. These probes are mostly based on chemical bonds with characteristic vibrational frequencies in the cell Raman-silent spectral window (1,800–2,700 cm^{-1} , Fig. 3a), offering desirable detection specificity and sensitivity. According to their sizes and applications, we divide them into three categories including vibrational tags (< 1 nm) for small-molecule imaging, Raman dye palettes (a few nm) for super-multiplexed imaging, and Raman-active nanomaterials (> 10 nm) (Fig. 3b).

Bioorthogonal chemical imaging. Although many fluorescence techniques are available for imaging biomacromolecules, such as proteins and nucleic acids, they are not readily applicable for imaging small biomolecules, which are key players in cell metabolism, signaling and regulation. This is largely because fluorophores, including fluorescent proteins and organic dyes, are much larger than small-molecule targets and thus could alter their native distribution, activity and interactions in cells. Much smaller, light-absorbing fluorophores do not exist, as determined by quantum mechanics (the particle in a box model).

To circumvent this limitation, vibrational tags with a few atoms—which exhibit a clear size advantage—including isotope-based and triple-bond based tags, have been actively developed for SRS imaging in the past decade. Besides reporting the spatial distribution of the tagged biomolecules, the exogenous tags can also reveal the metabolic turnover of labeled species in cells and provide additional temporal information, which is largely absent in label-free imaging of the steady-state. Therefore, SRS microscopy coupled with vibrational tags has allowed dynamic visualization of many small molecules in living systems with minimal perturbation, which has emerged as a new field of bioorthogonal chemical imaging^{63,64}.

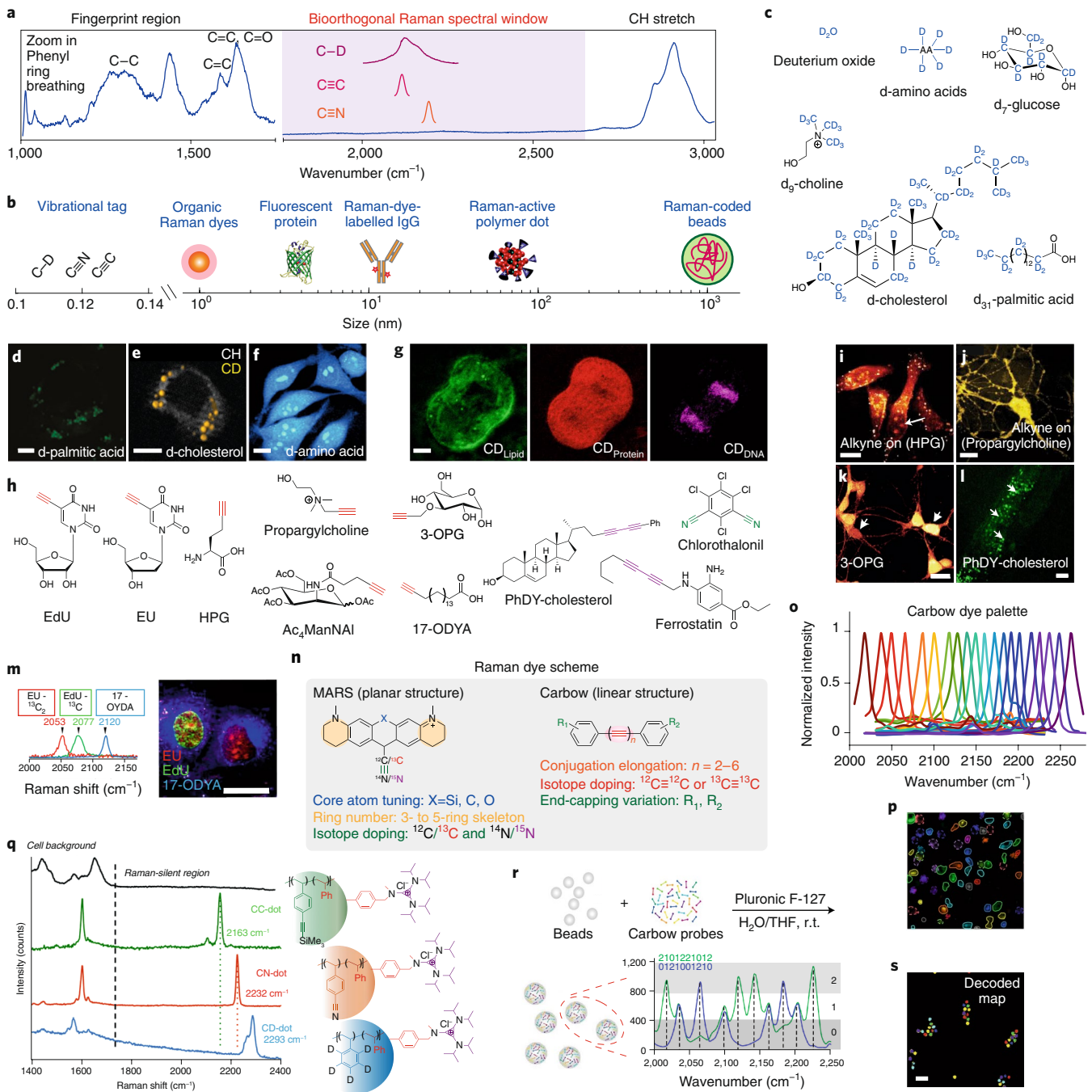


Fig. 3 | Imaging probe development. **a**, Typical cell Raman spectrum with the cell spectral-silent window where no Raman peak from endogenous biomolecules appears. **b**, Illustration of SRS imaging probes from small chemical bonds, to Raman dyes, to polymer dot, to coded beads. **c**, Chemical structures of small biomolecules with deuterium isotope labels. **d**, Imaging incorporation of d_3 -palmitic acid into lipid droplets and cell membrane. Scale bar, 5 μm . **e**, Imaging d_{38} -cholesterol uptake, esterification and storage inside lipid droplets. CD, carbon-deuterium bond; CH, carbon-hydrogen bond. Scale bar, 10 μm . **f**, Imaging of newly synthesized proteins by d-amino acids. Scale bar, 10 μm . **g**, D_2O labeling as a global metabolic tracer for newly synthesized proteins, lipids and DNA in live cells. Scale bar, 10 μm . **h**, Chemical structures of small biomolecules with triple-bond tags. **i**, Imaging of newly synthesized proteins by alkyne-tagged methionine analogue homopropargylglycine (HPG). Scale bar, 10 μm . **j**, Imaging of choline metabolites in neuron by propargylcholine. Scale bar, 10 μm . **k**, Imaging glucose uptake activity in live neurons by alkyne-tagged glucose analogue 3-OPG. Scale bar, 20 μm . **l**, Imaging of cholesterol storage in *C. elegans* with PhDY-cholesterol. Scale bar, 10 μm . **m**, Three-color imaging of EdU, EU and 17-ODYA with ^{13}C -edited alkyne probes. Scale bar, 25 μm . **n**, Schematic illustration of Raman dye structures for super-multiplexed imaging. **o**, Carbow dye palette with 20 well-resolved Raman peaks. **p**, Live-cell 16-color SRS-fluorescence tandem imaging with MARS and commercial dyes. **q**, Three-color Raman-active polymer dots by using monomers with small vibrational tags. **r**, Super-multiplexed barcoding by combinatory encoding of Carbow probes in polystyrene beads. **s**, Live-cell labeling and identification by SRS imaging of Carbow-coded beads. Scale bar, 10 μm .

Stable-isotope based vibrational tags. Stable isotopes, which are often used in nuclear magnetic resonance spectroscopy and mass spectrometry, are minimal labels and introduce little change to the

biochemical property of the molecular target. The main stable-isotope label used for SRS imaging is deuterium, which doubles the mass of hydrogen and significantly modifies the vibrational

frequency of associated chemical bonds for characteristic detection. For example, compared to C–H stretching at $\sim 2,900\text{ cm}^{-1}$, the carbon–deuterium bond (C–D) has a distinct frequency of $\sim 2,100\text{ cm}^{-1}$ in the cell silent region. Deuterium labels have thus been widely applied in SRS imaging of many species (Fig. 3c), including drugs⁶⁵, fatty acids⁶⁶, amino acids⁶⁷, choline⁶⁸, sterols⁶⁹ and glucose⁷⁰. Incorporation of fully deuterated d_{31} -palmitic acids to lipid droplets was first visualized by SRS in live cells⁶⁶ (Fig. 3d). Using d_{38} -cholesterol produced from an engineered yeast strain, heterogeneous cholesterol storage and esterification can be imaged in the lipid droplets of cells⁶⁹ (Fig. 3e). Moreover, SRS imaging of deuterated amino acids has achieved visualization of newly synthesized proteins in living cells, tissues and organisms^{67,71,72} (Fig. 3f).

To study cellular activity at a global level, deuterated water, D_2O , has been applied as a universal and cost-effective source of deuterium label to visualize in situ metabolism of proteins, lipids and DNA in cells, tissues and animals, by DO-SRS (ref. 73; Fig. 3g). In addition, glucose metabolism into biosynthesis can be traced using d_5 -glucose and spectral tracing of deuterium isotopes (STRIDE)⁷⁴. Moreover, with distinct Raman spectra of C–D bonds in proteins, lipids, DNA and glycogen, multiplexed imaging of biomass turnover can be monitored by both DO-SRS and STRIDE. In addition to deuterium, carbon isotope ^{13}C -labeled phenylalanine was also used to quantify protein synthesis and turnover dynamics by SRS imaging of the phenyl-ring breathing mode⁷⁵.

Triple-bond vibrational tags and their derivatives. Stable-isotope-based vibrational tags have minimal sizes but relatively moderate Raman intensity, and are suitable for high-abundant species. Triple bonds, such as alkyne (C \equiv C), diyne and nitrile (C \equiv N), also have sharp Raman peaks in the cell silent region and exhibit slightly larger sizes than isotope labels, but have much stronger Raman signal (1 alkyne is equivalent to ~ 30 C–D bonds in peak intensity). They were first utilized for spontaneous Raman microscopy^{76,77}. Unlike deuterated compounds, which are often commercially available, alkyne-tagged species usually require custom synthesis. As a small modification, an alkyne tag can be rationally incorporated to preserve the function of a target molecule. For SRS imaging of low abundant species with high specificity and sensitivity, triple-bond-based vibrational probes are particularly powerful, which has largely benefitted from the established field of bioorthogonal chemistry (mainly alkyne–azide click chemistry)^{78,79}.

A wide-range of small biomolecules have been visualized by SRS in living cells and tissues using single alkyne tags^{37,80}, including nucleosides, amino acids, choline, fatty acids, glycans⁸¹ and glucose⁸² (Fig. 3h). Homopropargylglycine (HPG) was developed as a methionine analogue to image protein synthesis based on the native translational machinery (Fig. 3i). Replacing a methyl group with a propargyl group is another approach for alkyne labeling, and propargylcholine can be used to visualize choline metabolism (Fig. 3j). 3-O-propargyl glucose (3-OPG), which can be recognized by glucose transporter, was developed to report glucose uptake activity in living cells and tissues⁸² (Fig. 3k). To further enhance the Raman signal of vibrational probes while still maintaining the small size, diyne tags with two conjugated triple bonds (Fig. 3h) were applied for SRS imaging of cholesterol⁸³ and small-molecule drugs such as ferrostatin⁸⁴, and can map their intracellular distributions and dynamics in live cells (Fig. 3l).

In addition, SRS imaging of multiple species can be achieved with alkyne tags. Given the vibrational frequency is inversely proportional to the square root of the reduced mass of the chemical bond, ^{13}C -edited alkyne tags were developed for three-color imaging of DNA, RNA and lipids in living mammalian cells⁸⁵ (Fig. 3m). Nitrile and isonitrile tags were also applied in SRS imaging of small molecules, such as fungicide chlorothalonil⁸⁶ (Fig. 3h) and bacterial metabolites rhabduscin⁸⁷, respectively.

Super-multiplexed Raman dyes and their palettes. Simultaneously visualizing a large number of molecules with high spatial and temporal resolution will allow system-level interrogation of the structure, function and dynamics of complex systems. Relying on the excitation and emission of electronic states, fluorescence spectra have broad linewidths ($\sim 50\text{ nm}$) due to the ultrashort dephasing time (in fs). Thus, fluorescence imaging is highly limited in multiplexed detection, allowing no more than 5–6 targets⁸⁸. This is often referred as the ‘color barrier’. Unlike fluorescence, Raman scattering probes the vibrational transition, which has a much longer dephasing time (in ps), with about 50–100-times narrower peak widths. Hence, in principle, Raman imaging can achieve much higher multiplexing capability. Leveraging the high sensitivity of SRS microscopy, super-multiplexed Raman dyes have been developed recently, breaking the color barrier in fluorescence and achieving direct imaging of tens of species in cells and tissues^{38,39}.

Two sets of Raman dyes are available to greatly expand the color palettes for super-multiplexed vibrational imaging (Fig. 3n–p). By conjugating alkynes and nitriles to near-infrared-absorbing xanthene, Manhattan Raman scattering (MARS) dyes achieved 14 well-resolved Raman peaks in the cell spectral-silent region³⁹, through changing the central atom (from O to C to Si) of xanthene, expanding the ring size in two-dimensions, and isotopic editing of alkynes and nitriles (Fig. 3n). Combined with the detection of six C=C bonds in the fingerprint region of commercial dyes, and four fluorescent channels, a total of 24 colors are accessible and were demonstrated in 16-color imaging of live-cell mixtures (Fig. 3p).

Another palette of super-multiplexed Raman dyes was developed based on the polyene scaffold³⁸. Polyene is a linear chain of conjugated alkynes, which has sharp Raman peaks, large intensity enhancement and natural frequency separation with increasing lengths. Through the chain-length modulation, bond-selective isotope labeling and end-group substitutions (Fig. 3n), 20 distinct Raman colors were obtained in the cell-silent window, which were termed the carbon rainbow (Carbow; Fig. 3o). With a neutral scaffold, Carbow probes are suitable for live-cell imaging with high membrane permeability and little non-specific background, such as in organelle-specific imaging. In addition, MARS dyes have superb sensitivity, down to sub- μM , under epr-SRS excitation, which are well suited for specific imaging of low-abundant molecules such as protein receptors and transcription factors. Thus, with the advent of MARS and Carbow palettes, super-multiplexed SRS microscopy has great potential in high-dimensional cell imaging and profiling to study complex biological systems.

Raman-active nanomaterials. Nanomaterials are widely used in biological imaging for sorting, disease diagnostics and drug delivery applications. Many nanomaterials have been developed, such as quantum dots, metal nanostructures, rare-earth nanocrystals and polymer nanoparticles. The hierarchical structures of nanoparticles provide unique benefits, including enhanced signal, tunable photophysics and versatile surface functionality, as well as physical carriers for storing substances and information, such as drugs and identities. Most contrasts in detecting nanomaterials are based on luminescence, which are limited by photobleaching, self-quenching, spectral crosstalk and low information content.

To overcome this, several Raman-active nanomaterials that are based on metal-free organic polymers have been developed for SRS imaging with high photostability, barcoding capacity and biocompatibility. Three-color Raman-active polymer dots (Fig. 3q) are imaged by SRS through incorporating small vibrational tags onto styrene monomers for mini-emulsion polymerization⁸⁹, which shows high stability, little cytotoxicity and fast endocytosis for live-cell sorting. Targeting groups, such as aptamers and peptides, can be further applied to achieve specific imaging of cell surface proteins

in living cells, tumor tissues and mice, based on poly(methacrylate) Raman beads⁹⁰.

Moreover, super-multiplexed optical barcoding can be achieved through combinatorial encoding of Carbow probes in polystyrene beads³⁸ (Fig. 3r), which can generate roughly 3^{10} –60,000 distinct spectral barcodes with little crosstalk for high-capacity cell labeling and rapid identification with SRS imaging (Fig. 3s). Thus, with the high biocompatibility, synthetic robustness and barcoding capability, Raman-active nanomaterials is useful for cell phenotyping in disease diagnostics and targeted drug delivery, as well as high-throughput in vitro screening and analysis by SRS.

Selected applications in biology and medicine

SRS microscopy has been used to generate important insights in many branches of biology. Here, we highlight applications in cell biology, lipid biology, microbiology, tumor biology, neurobiology, developmental biology and pharmaceuticals.

Cell biology. With both high spatial resolution and live-cell compatibility, SRS microscopy has been fruitful in studying cellular compositions and metabolism, revealing DNA, RNA, protein and glucose metabolism, and their turnover dynamics. As key genetic materials, label-free SRS imaging of DNA has been applied to visualize the chromosome dynamics at different stages of cell cycle⁵⁸ (Fig. 4a). Using ethynyl deoxyuridine (EdU), newly synthesized DNA can be directly imaged by SRS as a cell proliferation and division marker in tumor cells and neurons in brain tissues^{37,80}. RNA turnover dynamics was studied by SRS imaging of ethynyl uridine (EU), which showed a short lifetime of ~3 hours³⁷ (Fig. 4b).

Proteins are key players of cellular activity. Active sites of protein synthesis and degradation were identified inside living cells, through metabolic incorporation of deuterated amino acids^{67,71}. Two-color pulse-chase protein imaging by SRS further revealed the aggregate formation dynamics of huntingtin proteins in live cells⁷¹ (Fig. 4c). As an energy source for most life, glucose metabolism is also studied by SRS imaging. Alkyne-tagged glucose analogue (3-OPG) was developed to visualize uptake activities in tumor cells and neurons at the single-cell level⁸². Using both ¹³C-labeled 3-OPG and d₇-glucose, two-color imaging of glucose metabolism was achieved, which can report both glucose uptake and incorporation activities to show the heterogeneous patterns in glucose utilization between normal and cancerous cells⁹¹.

Harnessing the power of super-multiplexed Carbow probes, 10-color imaging of subcellular structures has been demonstrated in living HeLa cells (Fig. 4d), including mitochondria, lysosomes, endoplasmic reticulum, lipid droplets, plasma membrane, Golgi apparatus, microtubules, actins and nucleus³⁸. This technical demonstration can facilitate the study of inter-organelle contacts and interactions under both physiological and diseased conditions.

Lipid biology. Lipids are one of the most abundant species in cells, which include fatty acids, sterols and their derivatives. Lipid molecules, difficult to image by fluorescence due to their small sizes, have a strong and characteristic Raman signal both in the label-free approach and the bioorthogonal chemical imaging approach. As such, applications of SRS microscopy to lipid research have been particularly early and rich.

Lipid metabolism is closely associated to many metabolic diseases, such as atherosclerosis, obesity and diabetes. Using hyperspectral SRS imaging of CH₂ and C=C–H bonds to quantify neutral lipids, differential storages of triglycerides and cholesteryl esters in lipid droplets were found in different cells, tissues and metabolic disorders⁵⁷ (Fig. 4e). The incorporation of deuterated fatty acids was tracked to show unsaturated fatty acids preferentially in lipid droplets, while saturated fatty acids in both membrane structures and lipid droplets with higher toxicity in hepatic cells. A deeper

understanding of the lipotoxicity of saturated fatty acids was linked to the biophysics of the endoplasmic reticulum (ER) membrane⁹². By imaging the metabolism of deuterated fatty acids, saturated fatty acids including palmitic acids were found to induce a phase separation in the presumably fluidic ER membrane to form solid-like domains (Fig. 4f), the first to be observed in living cells, and suggested a role of the ER membrane phase in the onset of lipotoxicity.

In addition, lipid desaturation was found to be a metabolic marker in ovarian cancer by SRS imaging. An increased level of unsaturated lipids was observed in ovarian cancer stem cells (Fig. 4g), which was mediated by lipid desaturases and regulated through the NF- κ B survival pathway⁹³. Inhibition of lipid desaturation was shown to impair cancer stemness and suppress tumor formation in vivo. Moreover, by combining SRS imaging of lipids and fluorescent photo-highlighting, a high-throughput genetic screening method was developed to study lipid metabolism in *C. elegans* and identified 57 mutants with altered lipid phenotypes⁹⁴. Four mutants showed decreased lipid accumulation in somatic tissues (Fig. 4h), which was caused by inactivation of the bone morphogenetic protein (BMP) signaling pathway, and accelerated lipid catabolism through the induction of mitochondrial β -oxidation and fusion.

SRS imaging of sterol metabolism has also generated insights. By label-free SRS imaging of cholesterol ring vibration, high accumulation of cholesteryl ester was observed in advanced human prostate cancer tissues, induced by the loss of tumor suppressor PTEN, activation of the PI3K–AKT pathway and enhanced uptake of lipoproteins⁶⁰. Inhibition of cholesterol esterification was able to impair cancer aggressiveness. SRS imaging of phenyl-diyne-tagged cholesterol, an analogue with a stronger Raman signal, was applied to monitor cholesterol transport from lysosomes to lipid droplets in a cellular model of Niemann–Pick type C disease with 2-hydroxypropyl- β -cyclodextrin treatment⁸³.

Desmosterol was an important intermediate of cholesterol biosynthesis involved in the hepatitis C virus (HCV) replication during cell infection. SRS imaging of d6-desmosterol showed that they accumulated in lipid droplets closely associated with the viral NS5A protein⁹⁵, suggesting a direct effect on HCV replication. Squalene, another cholesterol precursor, was visualized by SRS to accumulate in the lipid droplets of cholesterol auxotrophic lymphoma cells⁹⁶ (Fig. 4i), as a result of the lack of squalene monooxygenase expression. Squalene accumulation was shown to protect cancer cells from ferroptotic cell death and provide a growth advantage under oxidative stress.

Microbiology. Microbiology has gained increasing attention due to its important roles in human gut microbiota, antibiotic resistance and biomaterials, such as biofuels. Rhabduscin, a metabolite produced by Gram-negative bacteria, was visualized by SRS to localize on the bacterial cell surface⁸⁷, where it could inhibit melanin-producing enzymes in insects as a possible mechanism to combat the host defense system. Label-free video-rate SRS imaging of *Euglena gracilis* was also used to map the intracellular metabolite distributions under different culture conditions¹⁶. Significant metabolic heterogeneity was observed in the live microalgae cultured under nitrogen-deficiency stress, with a reduced amount of chlorophyll, and increased accumulation of paramylon and lipids (Fig. 4j).

SRS imaging has also been applied to study antibiotic responses in bacterial biofilms, which cause drug-resistant infections in clinics. By tagging antibiotic vancomycin with an aryl-alkyne tag, SRS imaging can quantitatively monitor its penetration kinetics into biofilms, which showed a non-uniform diffusion with shallow depth due to preferential binding to the bacterial cells rather than the extracellular matrix⁹⁷. This provides a way to study the pharmacokinetics of antibiotic treatments in biofilms.

Moreover, SRS imaging has provided insights into the antibiotic tolerance and metabolic heterogeneity of *Pseudomonas aeruginosa*

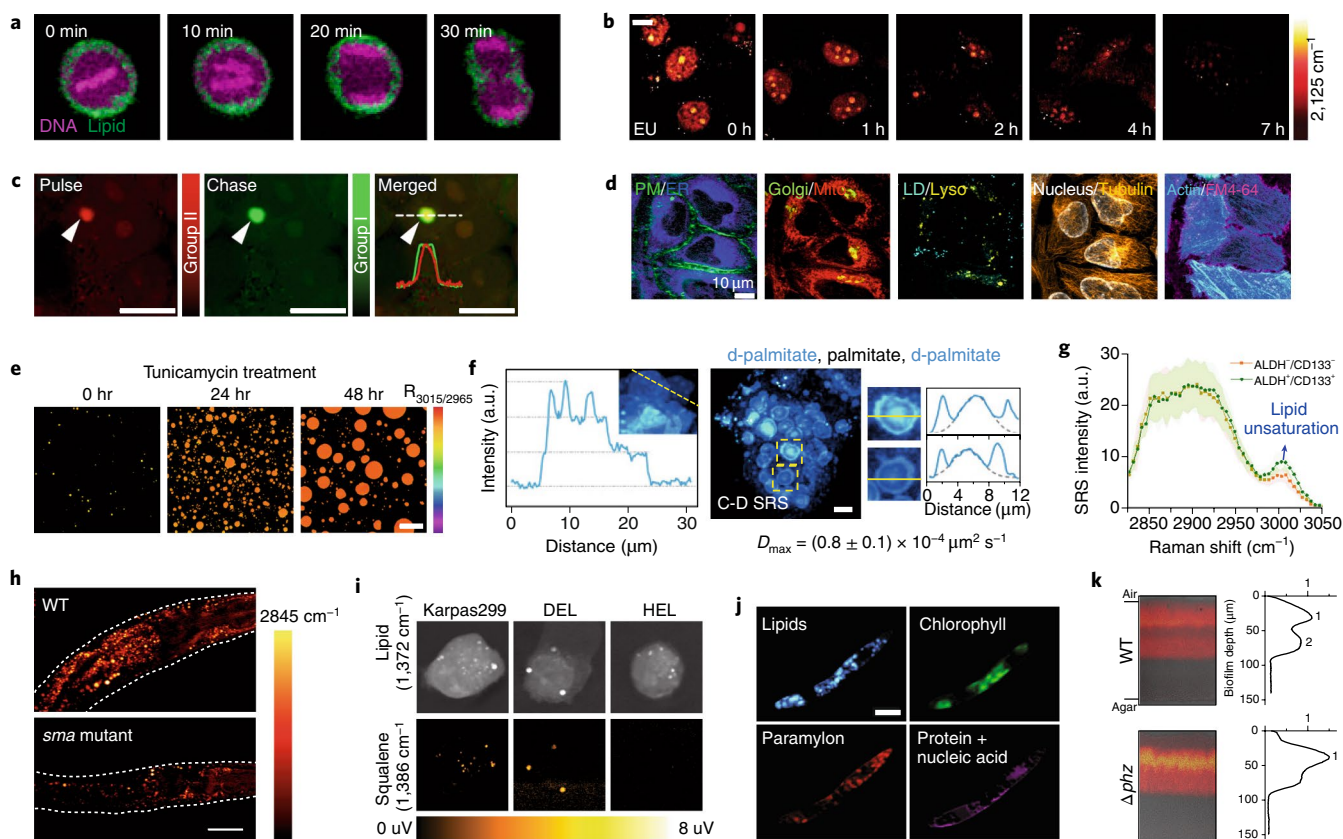


Fig. 4 | Application of SRS microscopy in cell biology, lipid biology and microbiology. **a**, Time-lapse label-free imaging of DNA in a HeLa cell undergoing cell division with SRS. **b**, Pulse-chase imaging of RNA turnover in HeLa cells with an alkyne-bearing nucleoside EU. Scale bar, 10 μm . **c**, Two-color pulse-chase imaging of newly synthesized proteins can be achieved by sequential labeling of group II and group I d-amino acids, which shows the dynamic formation process of mutant huntingtin protein aggregate in HeLa cells. Scale bar, 10 μm . **d**, 10-color organelle imaging in live HeLa cells with targeted Carbow probes. Scale bar, 10 μm . **e**, Lipid compositional changes associated with hepatic steatosis during ER stress by SRS imaging. The number and size of hepatic lipid droplets are dramatically increased in wild-type mice injected with ER stress-inducing drug tunicamycin in liver. Scale bar, 10 μm . **f**, SRS imaging with deuterated palmitic acids reveals solid-phase membrane in living cells with implications on lipotoxicity. Scale bar, 10 μm . **g**, Lipid desaturation is a metabolic marker of ovarian cancer stem cells. Non-stem cancer cells and cancer stem cells are found to have different intracellular lipid unsaturation level by probing the unsaturated C–H vibration (C=C–H) at $\sim 3,002\text{ cm}^{-1}$. **h**, Genetic screening of *C. elegans* with altered lipid phenotypes by combining photo-highlighting with SRS imaging, which shows BMP signaling inactivation regulates lipid metabolism through mitochondria homeostasis. Scale bar, 50 μm . **i**, SRS imaging reveals squalene accumulation in lipid droplets in anaplastic large cell lymphoma (ALCL) cells. **j**, Label-free video-rate SRS imaging shows heterogeneous distribution of metabolites in *E. gracilis* microalgae. Scale bar, 10 μm . **k**, SRS imaging of *Pseudomonas aeruginosa* biofilms, which reveals two distinct regions of metabolic activity.

biofilms, which are a major cause of chronic lung infections in cystic fibrosis patients. Through SRS imaging of D_2O incorporation, deep regions of active metabolism were observed for the first time in biofilms grown on glucose media⁹⁸ (Fig. 4k). In particular, the metabolic activity in the hypoxic region was linked to the small metabolites phenazines and Cco terminal oxidases, which support reduction–oxidation balancing in the oxygen-depleted environment and promote biofilm tolerance to antibiotics such as ciprofloxacin.

Tumor biology. Tumors are known to have unregulated proliferation with abnormal metabolism. Tumor heterogeneity further contributes to complications such as metastasis and cancer-therapy resistance. Studying tumor heterogeneity will allow a better understanding of the cause and progression of tumors for more effective diagnostics and treatments. SRS imaging has been applied to early characterization of tumors, especially in visualizing tumor boundaries and heterogeneity⁵⁵.

SRS imaging of intrinsic protein CH_3 and lipid CH_2 vibrations was first established as a label-free approach for in situ differentiation of tumor and healthy tissues in mouse models and human

tissues of glioblastoma (Fig. 5a), and showed a high correlation with standard hematoxylin and eosin (H&E) staining results^{54,99}. Intraoperative SRS imaging of fresh human brain tumor tissues was also achieved using a portable fiber-laser-based microscope, which revealed key structural heterogeneity in gliomas of different types (Fig. 5b). Moreover, machine-learning approaches were developed to classify brain tumor subtypes based on SRS images, with high accuracy¹⁰⁰.

Tumor metabolism was also studied by SRS imaging of vibrational probes. By imaging the metabolic incorporation of deuterated species, increased lipid synthesis was observed in the invasion front of breast cancer cell spheroids and infiltrating tumor cells in a mouse xenograft of glioblastoma⁵¹. The enhanced lipid incorporation was likely due to the epithelial-to-mesenchymal transition, which showed higher accumulation of lipid droplets in mesenchymal cells with bioorthogonal chemical imaging¹⁰¹. Furthermore, SRS imaging of protein and lipid synthesis using a D_2O probe can clearly visualize tumor boundaries and heterogeneity in a mouse xenograft of colon tumors⁷³ (Fig. 5c), which was difficult to distinguish using the label-free approach.

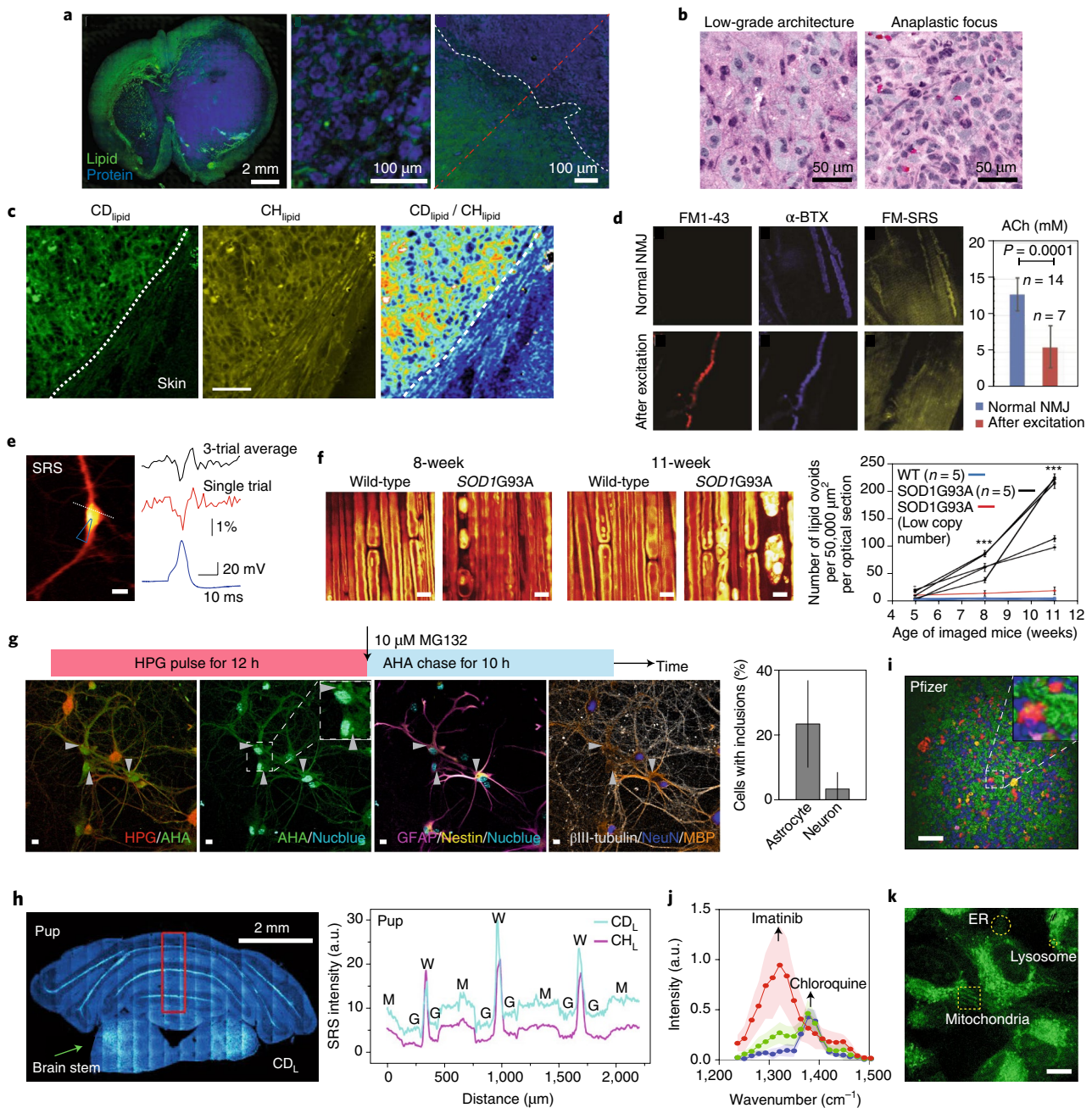


Fig. 5 | Application of SRS microscopy in tumor biology, neurobiology, developmental biology, and pharmaceuticals. a, Label-free SRS detection of brain tumors and tumor infiltration. Blue is protein channel and green is lipid channel. **b**, Structural heterogeneity in human brain tumors can be visualized by stimulated Raman pathology. **c**, Colon tumor boundary (dotted line) detection by dynamic metabolic imaging with DO-SRS. Scale bar, 20 μm . **d**, Direct imaging of local acetylcholine by SRS indicates a strong concentration decrease after electrical excitation at the neuromuscular junction of a frog cutaneous pectoris muscle. **e**, Single action potential can be captured by label-free SRS imaging on a patched neuron. Scale bar, 20 μm . **f**, Long-term in vivo imaging of peripheral nerve degeneration in ALS mouse models with SRS. Significant amounts of lipid ovoids were observed at early time points. Scale bar, 10 μm . **g**, Pulse-chase super-multiplexed SRS imaging in neuronal system under proteasomal stress. Protein aggregates are mostly found in astrocytes under proteasomal stress. Scale bar, 10 μm . **h**, Myelination development in pup mice visualized by STRIDE-SRS. M, molecular layer; G, granule cell layer; W, white matter. **i**, SRS imaging of active pharmaceutical ingredient (API) and excipients within tablets. Scale bar, 200 μm . **j**, SRS imaging of tyrosine kinase inhibitors. Quantifications of imatinib and chloroquine intensity indicate that chloroquine treatment reduces the trapping of imatinib in lysosomes. **k**, SRS imaging of subcellular distribution of ferrostatin-1 with a diyne tag which shows accumulation in ER, lysosomes and mitochondria. Scale bar, 10 μm .

Neurobiology. The nervous system plays several key roles in learning, memory, motion and behavior. The study of complex nervous systems in both physiological and degenerative states will help develop a holistic picture of neural functions and uncover the reasons behind neural disorders, where advanced imaging techniques are in great need.

SRS microscopy has also been applied to label-free imaging of neurotransmitters and membrane potentials. Using frequency-modulated spectral-focusing SRS, and the intrinsic C–N vibrations of choline, the local concentration of acetylcholine was directly determined to be ~ 10 mM at the neuromuscular junction of frog

cutaneous pectoris muscle¹⁰² (Fig. 5d). By label-free SRS imaging of a protein CH₃ Fermi resonance peak, puff-induced depolarizations of multiple neurons were visualized in live mouse brain tissues and single action potentials were detected in patched neurons¹⁰³ (Fig. 5e).

SRS microscopy has been further applied in studying brain pathologies, such as myelin degeneration in amyotrophic lateral sclerosis (ALS)¹⁰⁴ and amyloid plaques in Alzheimer's disease¹⁰⁵. Long-term SRS imaging of peripheral nerve degeneration showed the formation of lipid-rich ovoids at early time points in living ALS mouse models (Fig. 5f). Drug effects can also be monitored, facilitating early detection of ALS and potential interventions. Multicolor SRS microscopy also demonstrated label-free imaging of amyloid plaques in Alzheimer's disease. By utilizing the frequency shift of protein amide I band in β -sheet structures, misfolded amyloid- β plaques were visualized in both frozen and fresh brain tissues from an APP:PS1 mouse model of Alzheimer's disease, which was consistent with conventional immunohistochemistry and thioflavin S staining results.

Using alkyne and deuterium tags, bioorthogonal chemical imaging of metabolic activities was also achieved in live rat brain tissues, showing heterogeneous patterns of DNA, RNA, protein and lipid metabolisms. In particular, increased lipid synthesis was observed in the hilus region of the hippocampus after mechanical stretching in a traumatic brain injury model⁸⁰. The development of supermultiplexed MARS probes further allowed 8-color imaging of complex metabolic activity in neuronal co-culture and mouse brain tissues³⁹ (Fig. 5g). Cell-type-dependent metabolic heterogeneities were revealed, with astrocytes forming more proteome inclusions than neurons under proteasomal stress, suggesting an active role by sequestering misfolded protein species.

Developmental biology. Organism developments involve active metabolism with enhanced biosynthesis. Several metabolic probes, such as deuterated amino acids, d₅-choline, D₂O and d₇-glucose, have been applied in studying protein and lipid metabolism in the developments of multiple organisms, including *Caenorhabditis elegans*, zebrafish and mice^{68,71–74}. In *C. elegans*, label-free imaging of retinoids showed a previously unknown cytoplasmic reservoir, which increased with developmental time and was shown to regulate fat storage, especially in dauer larvae¹⁰⁶.

To probe development more generally, D₂O was applied to study lipid synthesis in germline development of *C. elegans*, and myelination dynamics in developing mouse brain⁷³. Zebrafish embryogenesis was also visualized with DO-SRS, which showed a much faster rate of protein synthesis than lipogenesis during embryonic cell division. Combined with lineage-specific fluorescent markers, metabolic activities of particular cell types can be imaged during lineage progression. Furthermore, STRIDE-SRS using d₇-glucose revealed strong patterns of lipid turnover in the cerebellum of young mouse brain (Fig. 5h), which was correlated with the expression of myelin basic proteins during the myelination process⁷⁴.

Pharmaceuticals. Visualizing pharmaceutical compounds in the regulation of cellular activity in living systems is important to understand their mechanism of action. SRS microscopy has been applied for drug imaging using both a label-free approach and small vibrational tags¹⁰⁷. The imaging result can contribute to the understanding of the structure–distribution–function relationship, which can in turn facilitate more effective drug discovery and development.

With intrinsically strong vibrational contrasts, SRS has achieved imaging of drug formulation in tablets and implants^{108,109}, agrochemical compounds in antifungal treatments of plants^{86,110}, and dermal drug delivery^{35,37,65}, as well as subcellular distribution of small-molecule drugs¹¹¹. Epi-SRS microscopy was applied to examine amlodipine besylate tablets from six commercial sources, and

showed different compositions and distribution of excipients¹⁰⁸ (Fig. 5i)—information that could be used in formulation screening for optimized drug release. With hyperspectral SRS microscopy, several tyrosine kinase inhibitors, including imatinib, nilotinib and GNF-2/5, were imaged quantitatively inside living cells¹¹¹. Both imatinib and nilotinib were found to be strongly enriched in the lysosomes, and cotreatment of chloroquine was shown to reduce the lysosomal trapping of imatinib by more than tenfold (Fig. 5j), which could contribute to the enhanced drug efficacy.

For drugs without characteristic vibrational features, small Raman tags were applied for SRS imaging with improved sensitivity and specificity. Deuterium labels were applied to visualize the penetration of ibuprofen⁶⁵ and several pharmaceutically relevant solvents¹¹² in skin and nails, respectively. Triple-bond tags have also been applied to study the intracellular distribution and dynamics of small molecule inhibitors, including anisomycin¹¹³, antimycins¹¹⁴ and ferrostatins⁸⁴. Diyne-tagged ferrostatin-1, a potent inhibitor of ferroptosis, was imaged by SRS in live cells and shown to mainly accumulate in lysosomes, mitochondria and ER (Fig. 5k). Functional experiments using lysosomal targeting and mitophagy showed that neither organelle was the primary site for ferroptosis protection, suggesting the ER as a likely site for ferrostatin action.

Outlook

The field of SRS microscopy has grown tremendously in the last ten years, and attracted increasingly more attention from the life sciences community. Continuing developments in spectroscopy and microscopy will render SRS an even more powerful bio-imaging platform in the foreseeable future. Further improvements in the detection sensitivity and spatial resolution of SRS are likely to be important moving forward. A promising direction is to combine the increased hyperpolarizability of conjugated systems with electronic-resonance, such as including the structure of conjugated alkynes in chromophores. In addition to signal enhancement, the electronic-resonance condition can be further modulated, spatially or temporally, to break the diffraction limit. Moreover, as a highly efficient way to excite molecular vibration, SRS can be coupled to other physical processes and observables, such as photothermal microscopy^{115,116}, optical coherence tomography¹¹⁷, photo-induced force microscopy¹¹⁸ and atomic force microscopy¹¹⁹, which could offer benefits in terms of sensitivity, penetration or resolution. For example, SRS has been successfully coupled to fluorescence in SREF microscopy to achieve vibrational imaging of single molecules⁴⁰.

Imaging probes serve as critical mediators in light-matter interactions that not only report the spatiotemporal information of the target of interest but also provide new functions, such as pseudocoloring and sensing. While super-multiplexed SRS imaging with 24 colors has been achieved with MARS and Carbow dyes^{38,39}, more vibrational colors are accessible by utilizing the entire cell-silent window, through novel chemical bond engineering or applying additional criteria to resolve vibrational frequency. For example, both vibrational and electronic resonances can be harnessed to define a 'color' in a two-dimensional spectrum. In addition, vibrational sensors can be developed by incorporating moieties that are responsive to external physical and chemical stimuli, including light, voltage and reactive species in cells. In fact, a ratiometric Raman sensor has been recently reported to use SRS to detect H₂S in the mitochondria of living cells¹²⁰. Furthermore, genetically encodable Raman probes, which will allow in situ protein and nucleic acid imaging in living cells with genetic specificity, are greatly needed. A recent report demonstrated SRS imaging of histone proteins in fixed cells, albeit with limited sensitivity, by using an alkyne-bearing unnatural amino acid and genetic code expansion approach¹²¹. Another direction is to engineer genetically encoded proteins and aptamers that can bind to vibrational probes for in situ imaging.

Lastly, in the era of systems biology, bridging the rich chemical information in broadband Raman spectrum with genomics, transcriptomics and proteomics, as well as metabolomics, could allow SRS to achieve large-scale cell profiling in a top-down and cost-effective way. High-throughput high-speed Raman flow cytometry has been demonstrated to reach a throughput of $\sim 2,000$ cells s^{-1} (refs. ^{33,122,123}). The massive amount of Raman data also requires the development of advanced statistical tools, such as dimension reduction and correlation, which can benefit from the field of machine learning. Looking forward, we envision that advanced SRS imaging and analysis will be a major force in future biological discovery.

Received: 8 March 2019; Accepted: 23 July 2019;

Published online: 30 August 2019

References

- Ploetz, E., Laimgruber, S., Berner, S., Zinth, W. & Gilch, P. Femtosecond stimulated Raman microscopy. *Appl. Phys. B* **87**, 389–393 (2007).
- Freudiger, C. W. et al. Label-free biomedical imaging with high sensitivity by stimulated Raman scattering microscopy. *Science* **322**, 1857–1861 (2008).
- Nandakumar, P., Kovalev, A. & Volkmer, A. Vibrational imaging based on stimulated Raman scattering microscopy. *New J. Phys.* **11**, 033026 (2009).
- Ozeki, Y., Dake, E., Kajiyama, S., Fukui, K. & Itoh, K. Analysis and experimental assessment of the sensitivity of stimulated Raman scattering microscopy. *Opt. Express* **17**, 3651–3658 (2009).
- Bloembergen, N. The stimulated Raman effect. *Am. J. Phys.* **35**, 989 (1967).
- Owyong, A. Sensitivity limitations for CW stimulated Raman spectroscopy. *Opt. Commun.* **22**, 323–328 (1977).
- Levine, B. E., Shank, C. V. & Heritage, J. P. Surface vibrational spectroscopy using stimulated Raman-scattering. *IEEE J. Quantum Elect.* **15**, 1418–1432 (1979).
- Levenson, M. D. & Kano, S. S. *Introduction to Nonlinear Laser Spectroscopy* (Acad. Press, 1988).
- Kukura, P., McCamant, D. W. & Mathies, R. A. Femtosecond stimulated Raman spectroscopy. *Annu. Rev. Phys. Chem.* **58**, 461–488 (2007).
- Min, W., Freudiger, C. W., Lu, S. J. & Xie, X. S. Coherent nonlinear optical imaging: beyond fluorescence microscopy. *Annu. Rev. Phys. Chem.* **62**, 507–530 (2011).
- Cheng, J. X. & Xie, X. S. Vibrational spectroscopic imaging of living systems: an emerging platform for biology and medicine. *Science* **350**, aaa8870 (2015).
- Camp, C. H. & Cicerone, M. T. Chemically sensitive bioimaging with coherent Raman scattering. *Nat. Photon.* **9**, 295–305 (2015).
- Prince, R. C., Frontiera, R. R. & Potma, E. O. Stimulated Raman scattering: from bulk to nano. *Chem. Rev.* **117**, 5070–5094 (2017).
- Saar, B. G. et al. Video-rate molecular imaging in vivo with stimulated Raman scattering. *Science* **330**, 1368–1370 (2010).
- Ozeki, Y. et al. High-speed molecular spectral imaging of tissue with stimulated Raman scattering. *Nat. Photon.* **6**, 844–850 (2012).
- Wakisaka, Y. et al. Probing the metabolic heterogeneity of live *Euglena gracilis* with stimulated Raman scattering microscopy. *Nat. Microbiol.* **1**, 16124 (2016).
- Freudiger, C. W. et al. Stimulated Raman scattering microscopy with a robust fibre laser source. *Nat. Photon.* **8**, 153–159 (2014).
- Kong, L. et al. Multicolor stimulated Raman scattering microscopy with a rapidly tunable optical parametric oscillator. *Opt. Lett.* **38**, 145–147 (2013).
- Suhalim, J. L. et al. Characterization of cholesterol crystals in atherosclerotic plaques using stimulated Raman scattering and second-harmonic generation microscopy. *Biophys. J.* **102**, 1988–1995 (2012).
- Freudiger, C. W. et al. Highly specific label-free molecular imaging with spectrally tailored excitation stimulated Raman scattering (STE-SRS) microscopy. *Nat. Photon.* **5**, 103–109 (2011).
- Zhang, D. et al. Quantitative vibrational imaging by hyperspectral stimulated Raman scattering microscopy and multivariate curve resolution analysis. *Anal. Chem.* **85**, 98–106 (2013).
- Andresen, E. R., Berto, P. & Rigneault, H. Stimulated Raman scattering microscopy by spectral focusing and fiber-generated soliton as Stokes pulse. *Opt. Lett.* **36**, 2387–2389 (2011).
- Fu, D., Holtom, G., Freudiger, C., Zhang, X. & Xie, X. S. Hyperspectral imaging with stimulated Raman scattering by chirped femtosecond lasers. *J. Phys. Chem. B* **117**, 4634–4640 (2013).
- He, R. Y. et al. Stimulated Raman scattering microscopy and spectroscopy with a rapid scanning optical delay line. *Opt. Lett.* **42**, 659–662 (2017).
- Alshaykh, M. S. et al. High-speed stimulated hyperspectral Raman imaging using rapid acousto-optic delay lines. *Opt. Lett.* **42**, 1548–1551 (2017).
- Liao, C. S. et al. Stimulated Raman spectroscopic imaging by microsecond delay-line tuning. *Optica* **3**, 1377–1380 (2016).
- Figuerola, B. et al. Broadband hyperspectral stimulated Raman scattering microscopy with a parabolic fiber amplifier source. *Biomed. Opt. Exp.* **9**, 6116–6131 (2018).
- He, R. Y. et al. Dual-phase stimulated Raman scattering microscopy for real-time two-color imaging. *Optica* **4**, 44–47 (2017).
- Lu, F. K. et al. Multicolor stimulated Raman scattering (SRS) microscopy. *Mol. Phys.* **110**, 1927–1932 (2012).
- Seto, K., Okuda, Y., Tokunaga, E. & Kobayashi, T. Development of a multiplex stimulated Raman microscope for spectral imaging through multi-channel lock-in detection. *Rev. Sci. Instrum.* **84**, 083705 (2013).
- Rock, W., Bonn, M. & Parekh, S. H. Near shot-noise limited hyperspectral stimulated Raman scattering spectroscopy using low energy lasers and a fast CMOS array. *Opt. Express* **21**, 15113–15120 (2013).
- Liao, C. S. et al. Microsecond scale vibrational spectroscopic imaging by multiplex stimulated Raman scattering microscopy. *Light Sci. Appl.* **4**, e265 (2015).
- Zhang, C. et al. Stimulated Raman scattering flow cytometry for label-free single-particle analysis. *Optica* **4**, 103–109 (2017).
- Fu, D. et al. Quantitative chemical imaging with multiplex stimulated Raman scattering microscopy. *J. Am. Chem. Soc.* **134**, 3623–3626 (2012).
- Liao, C. S. et al. Spectrometer-free vibrational imaging by retrieving stimulated Raman signal from highly scattered photons. *Sci. Adv.* **1**, e1500738 (2015).
- Saltarelli, F. et al. Broadband stimulated Raman scattering spectroscopy by a photonic time stretcher. *Opt. Exp.* **24**, 21264–21275 (2016).
- Wei, L. et al. Live-cell imaging of alkyne-tagged small biomolecules by stimulated Raman scattering. *Nat. Meth.* **11**, 410–412 (2014).
- Hu, F. et al. Supermultiplexed optical imaging and barcoding with engineered polyynes. *Nat. Meth.* **15**, 194–200 (2018).
- Wei, L. et al. Super-multiplex vibrational imaging. *Nature* **544**, 465–470 (2017).
- Xiong, H. et al. Stimulated Raman excited fluorescence spectroscopy and imaging. *Nat. Photon.* **13**, 412–417 (2019).
- Frontiera, R. R., Henry, A. L., Gruenke, N. L. & Van Duyne, R. P. Surface-enhanced femtosecond stimulated Raman spectroscopy. *J. Phys. Chem. Lett.* **2**, 1199–1203 (2011).
- Yampolsky, S. et al. Seeing a single molecule vibrate through time-resolved coherent anti-Stokes Raman scattering. *Nat. Photon.* **8**, 650–656 (2014).
- Zong, C. et al. Plasmon-enhanced stimulated Raman scattering microscopy with single-molecule detection sensitivity. Preprint at *arXiv* <https://arxiv.org/abs/1903.05167> (2019).
- Bi, Y. et al. Near-resonance enhanced label-free stimulated Raman scattering microscopy with spatial resolution near 130 nm. *Light Sci. Appl.* **7**, 81 (2018).
- Gong, L. & Wang, H. Breaking the diffraction limit by saturation in stimulated-Raman-scattering microscopy: a theoretical study. *Phys. Rev. A* **90**, 013818 (2014).
- Gong, L. & Wang, H. F. Suppression of stimulated Raman scattering by an electromagnetically-induced-transparency-like scheme and its application for super-resolution microscopy. *Phys. Rev. A* **92**, 023828 (2015).
- Kim, D. et al. Selective suppression of stimulated Raman scattering with another competing stimulated Raman scattering. *J. Phys. Chem. Lett.* **8**, 6118–6123 (2017).
- Hell, S. W. & Wichmann, J. Breaking the diffraction resolution limit by stimulated emission: stimulated-emission-depletion fluorescence microscopy. *Opt. Lett.* **19**, 780–782 (1994).
- Silva, W. R., Graefe, C. T. & Frontiera, R. R. Toward label-free super-resolution microscopy. *ACS Photon.* **3**, 79–86 (2016).
- Gong, L., Zheng, W., Ma, Y. & Huang, Z. W. Saturated stimulated-Raman-scattering microscopy for far-field superresolution vibrational imaging. *Phys. Rev. Appl.* **11**, 034041 (2019).
- Wei, M. et al. Volumetric chemical imaging by clearing-enhanced stimulated Raman scattering microscopy. *Proc. Natl. Acad. Sci. USA* **116**, 6608–6617 (2019).
- Chen, X. L. et al. Volumetric chemical imaging by stimulated Raman projection microscopy and tomography. *Nat. Commun.* **8**, 15117 (2017).
- Liao, C. S. et al. In vivo and in situ spectroscopic imaging by a handheld stimulated Raman scattering microscope. *ACS Photon.* **5**, 947–954 (2018).
- Ji, M. et al. Rapid, label-free detection of brain tumors with stimulated Raman scattering microscopy. *Sci. Transl. Med.* **5**, 201ra119 (2013).
- Freudiger, C. W. et al. Multicolored stain-free histopathology with coherent Raman imaging. *Lab. Investig.* **92**, 1492–1502 (2012).
- Wang, M. C., Min, W., Freudiger, C. W., Ruvkun, G. & Xie, X. S. RNAi screening for fat regulatory genes with SRS microscopy. *Nat. Meth.* **8**, 135–138 (2011).
- Fu, D. et al. In vivo metabolic fingerprinting of neutral lipids with hyperspectral stimulated Raman scattering microscopy. *J. Am. Chem. Soc.* **136**, 8820–8828 (2014).

58. Lu, F. K. et al. Label-free DNA imaging *in vivo* with stimulated Raman scattering microscopy. *Proc. Natl. Acad. Sci. USA* **112**, 11624–11629 (2015).
59. Wang, P. et al. Label-free quantitative imaging of cholesterol in intact tissues by hyperspectral stimulated Raman scattering microscopy. *Angew. Chem. Int. Ed. Engl.* **52**, 13042–13046 (2013).
60. Yue, S. et al. Cholesteryl ester accumulation induced by PTEN loss and PI3K/AKT activation underlies human prostate cancer aggressiveness. *Cell Metab.* **19**, 393–406 (2014).
61. Saar, B. G. et al. Label-free, real-time monitoring of biomass processing with stimulated Raman scattering microscopy. *Angew. Chem. Int. Ed. Engl.* **49**, 5476–5479 (2010).
62. Ding, S. Y. et al. How does plant cell wall nanoscale architecture correlate with enzymatic digestibility? *Science* **338**, 1055–1060 (2012).
63. Wei, L. et al. Live-cell bioorthogonal chemical imaging: stimulated Raman scattering microscopy of vibrational probes. *Acc. Chem. Res.* **49**, 1494–1502 (2016).
64. Shen, Y., Hu, F. & Min, W. Raman imaging of small biomolecules. *Annu. Rev. Biophys.* **48**, 347–369 (2019).
65. Saar, B. G., Contreras-Rojas, L. R., Xie, X. S. & Guy, R. H. Imaging drug delivery to skin with stimulated Raman scattering microscopy. *Mol. Pharma.* **8**, 969–975 (2011).
66. Zhang, D., Slipchenko, M. N. & Cheng, J. X. Highly sensitive vibrational imaging by femtosecond pulse stimulated Raman loss. *J. Phys. Chem. Lett.* **2**, 1248–1253 (2011).
67. Wei, L., Yu, Y., Shen, Y., Wang, M. C. & Min, W. Vibrational imaging of newly synthesized proteins in live cells by stimulated Raman scattering microscopy. *Proc. Natl. Acad. Sci. USA* **110**, 11226–11231 (2013).
68. Hu, F., Wei, L., Zheng, C., Shen, Y. & Min, W. Live-cell vibrational imaging of choline metabolites by stimulated Raman scattering coupled with isotope-based metabolic labeling. *Analyst* **139**, 2312–2317 (2014).
69. Alfonso-Garcia, A., Pfisterer, S. G., Riezman, H., Ikonen, E. & Potma, E. O. D38-cholesterol as a Raman active probe for imaging intracellular cholesterol storage. *J. Biomed. Opt.* **21**, 061003 (2016).
70. Li, J. & Cheng, J. X. Direct visualization of *de novo* lipogenesis in single living cells. *Sci. Rep.* **4**, 6807 (2014).
71. Wei, L. et al. Imaging complex protein metabolism in live organisms by stimulated Raman scattering microscopy with isotope labeling. *ACS Chem. Biol.* **10**, 901–908 (2015).
72. Shi, L. Y., Shen, Y. H. & Min, W. Visualizing protein synthesis in mice with *in vivo* labeling of deuterated amino acids using vibrational imaging. *Appl. Photon.* **3**, 092401 (2018).
73. Shi, L. et al. Optical imaging of metabolic dynamics in animals. *Nat. Commun.* **9**, 2995 (2018).
74. Zhang, L. et al. Spectral tracing of isotope deuterium (STRIDE) for imaging glucose metabolism. *Nat. Biomed. Eng.* **3**, 402–413 (2019).
75. Shen, Y., Xu, F., Wei, L., Hu, F. & Min, W. Live-cell quantitative imaging of proteome degradation by stimulated Raman scattering. *Angew. Chem. Int. Ed. Engl.* **53**, 5596–5599 (2014).
76. Yamakoshi, H. et al. Imaging of EdU, an alkyne-tagged cell proliferation probe, by Raman microscopy. *J. Am. Chem. Soc.* **133**, 6102–6105 (2011).
77. Yamakoshi, H. et al. Alkyne-tag Raman imaging for visualization of mobile small molecules in live cells. *J. Am. Chem. Soc.* **134**, 20681–20689 (2012).
78. Prescher, J. A. & Bertozzi, C. R. Chemistry in living systems. *Nat. Chem. Biol.* **1**, 13–21 (2005).
79. Grammel, M. & Hang, H. C. Chemical reporters for biological discovery. *Nat. Chem. Biol.* **9**, 475–484 (2013).
80. Hu, F., Lamprecht, M. R., Wei, L., Morrison, B. & Min, W. Bioorthogonal chemical imaging of metabolic activities in live mammalian hippocampal tissues with stimulated Raman scattering. *Sci. Rep.* **6**, 39660 (2016).
81. Hong, S. et al. Live-cell stimulated Raman scattering imaging of alkyne-tagged biomolecules. *Angew. Chem. Int. Ed. Engl.* **53**, 5827–5831 (2014).
82. Hu, F. et al. Vibrational imaging of glucose uptake activity in live cells and tissues by stimulated Raman scattering. *Angew. Chem. Int. Ed. Engl.* **54**, 9821–9825 (2015).
83. Lee, H. J. et al. Assessing cholesterol storage in live cells and *C. elegans* by stimulated Raman scattering imaging of phenyl-Diyne cholesterol. *Sci. Rep.* **5**, 7930 (2015).
84. Gaschler, M. M. et al. Determination of the subcellular localization and mechanism of action of ferrostatins in suppressing ferroptosis. *ACS Chem. Biol.* **13**, 1013–1020 (2018).
85. Chen, Z. et al. Multicolor live-cell chemical imaging by isotopically edited alkyne vibrational palette. *J. Am. Chem. Soc.* **136**, 8027–8033 (2014).
86. Mansfield, J. C. et al. Label-free chemically specific imaging in planta with stimulated Raman scattering microscopy. *Anal. Chem.* **85**, 5055–5063 (2013).
87. Crawford, J. M., Portmann, C., Zhang, X., Roeffaers, M. B. & Clardy, J. Small molecule perimeter defense in entomopathogenic bacteria. *Proc. Natl. Acad. Sci. USA* **109**, 10821–10826 (2012).
88. Valm, A. M. et al. Applying systems-level spectral imaging and analysis to reveal the organelle interactome. *Nature* **546**, 162–167 (2017).
89. Hu, F., Brucks, S. D., Lambert, T. H., Campos, L. M. & Min, W. Stimulated Raman scattering of polymer nanoparticles for multiplexed live-cell imaging. *Chem. Commun.* **53**, 6187–6190 (2017).
90. Jin, Q. et al. Multicolor Raman beads for multiplexed tumor cell and tissue imaging and *in vivo* tumor spectral detection. *Anal. Chem.* **91**, 3784–3789 (2019).
91. Long, R. et al. Two-color vibrational imaging of glucose metabolism using stimulated Raman scattering. *Chem. Commun.* **54**, 152–155 (2018).
92. Shen, Y. et al. Metabolic activity induces membrane phase separation in endoplasmic reticulum. *Proc. Natl. Acad. Sci. USA* **114**, 13394–13399 (2017).
93. Li, J. J. et al. Lipid desaturation is a metabolic marker and therapeutic target of ovarian cancer stem cells. *Cell Stem Cell* **20**, 303–314 (2017).
94. Yu, Y., Mutlu, A. S., Liu, H. & Wang, M. C. High-throughput screens using photo-highlighting discover BMP signaling in mitochondrial lipid oxidation. *Nat. Commun.* **8**, 865 (2017).
95. Villareal, V. A., Fu, D., Costello, D. A., Xie, X. S. & Yang, P. L. Hepatitis C virus selectively alters the intracellular localization of desmosterol. *ACS Chem. Biol.* **11**, 1827–1833 (2016).
96. Garcia-Bermudez, J. et al. Squalene accumulation in cholesterol auxotrophic lymphomas prevents oxidative cell death. *Nature* **567**, 118–122 (2019).
97. Bae, K., Zheng, W., Ma, Y. & Huang, Z. Real-time monitoring of pharmacokinetics of antibiotics in biofilms with Raman-tagged hyperspectral stimulated Raman scattering microscopy. *Theranostics* **9**, 1348–1357 (2019).
98. Schiessl, K. T. et al. Phenazine production promotes antibiotic tolerance and metabolic heterogeneity in *Pseudomonas aeruginosa* biofilms. *Nat. Commun.* **10**, 762 (2019).
99. Ji, M. et al. Detection of human brain tumor infiltration with quantitative stimulated Raman scattering microscopy. *Sci. Transl. Med.* **7**, 309ra163 (2015).
100. Orringer, D. A. et al. Rapid intraoperative histology of unprocessed surgical specimens via fibre-laser-based stimulated Raman scattering microscopy. *Nat. Biomed. Eng.* **1**, 0027 (2017).
101. Zhang, L. Y. & Min, W. Bioorthogonal chemical imaging of metabolic changes during epithelial-mesenchymal transition of cancer cells by stimulated Raman scattering microscopy. *J. Biomed. Opt.* **22**, 106010 (2017).
102. Fu, D., Yang, W. & Xie, X. S. Label-free imaging of neurotransmitter acetylcholine at neuromuscular junctions with stimulated Raman scattering. *J. Am. Chem. Soc.* **139**, 583–586 (2017).
103. Lee, H. J. et al. Label-free vibrational spectroscopic imaging of neuronal membrane potential. *J. Phys. Chem. Lett.* **8**, 1932–1936 (2017).
104. Tian, F. et al. Monitoring peripheral nerve degeneration in ALS by label-free stimulated Raman scattering imaging. *Nat. Commun.* **7**, 13283 (2016).
105. Ji, M. et al. Label-free imaging of amyloid plaques in Alzheimer's disease with stimulated Raman scattering microscopy. *Sci. Adv.* **4**, eaat7715 (2018).
106. Chen, A. J. et al. Fingerprint stimulated Raman scattering imaging reveals retinoid coupling lipid metabolism and survival. *Chem. Phys. Chem.* **19**, 2500–2506 (2018).
107. Tipping, W. J., Lee, M., Serrels, A., Brunton, V. G. & Hulme, A. N. Stimulated Raman scattering microscopy: an emerging tool for drug discovery. *Chem. Soc. Rev.* **45**, 2075–2089 (2016).
108. Slipchenko, M. N. et al. Vibrational imaging of tablets by epi-detected stimulated Raman scattering microscopy. *Analyst* **135**, 2613–2619 (2010).
109. Francis, A. T. et al. *In situ* stimulated Raman scattering (SRS) microscopy study of the dissolution of sustained-release implant formulation. *Mol. Pharma.* **15**, 5793–5801 (2018).
110. Wang, C. C. et al. *In situ* chemically specific mapping of agrochemical seed coatings using stimulated Raman scattering microscopy. *J. Biophoton.* **11**, e201800108 (2018).
111. Fu, D. et al. Imaging the intracellular distribution of tyrosine kinase inhibitors in living cells with quantitative hyperspectral stimulated Raman scattering. *Nat. Chem.* **6**, 614–622 (2014).
112. Chiu, W. S. et al. Molecular diffusion in the human nail measured by stimulated Raman scattering microscopy. *Proc. Natl. Acad. Sci. USA* **112**, 7725–7730 (2015).
113. Tipping, W. J., Lee, M., Serrels, A., Brunton, V. G. & Hulme, A. N. Imaging drug uptake by bioorthogonal stimulated Raman scattering microscopy. *Chem. Sci.* **8**, 5606–5615 (2017).
114. Seidel, J. et al. Structure-activity-distribution relationship study of anti-cancer antimycin-type depsipeptides. *Chem. Commun.* <https://doi.org/10.1039/c9cc03051d> (2019).
115. Gaiduk, A., Yorulmaz, M., Ruijgrok, P. V. & Orrit, M. Room-temperature detection of a single molecule's absorption by photothermal contrast. *Science* **330**, 353–356 (2010).
116. Zhang, D. et al. Depth-resolved mid-infrared photothermal imaging of living cells and organisms with submicrometer spatial resolution. *Sci. Adv.* **2**, e1600521 (2016).

117. Robles, F. E., Zhou, K. C., Fischer, M. C. & Warren, W. S. Stimulated Raman scattering spectroscopic optical coherence tomography. *Optica* **4**, 243–246 (2017).
118. Tamma, V. A., Beecher, L. M., Shumaker-Parry, J. S. & Wickramasinghe, H. K. Detecting stimulated Raman responses of molecules in plasmonic gap using photon induced forces. *Opt. Exp.* **26**, 31439–31453 (2018).
119. Knoll, B. & Keilmann, F. Near-field probing of vibrational absorption for chemical microscopy. *Nature* **399**, 134–137 (1999).
120. Zeng, C., Hu, F., Long, R. & Min, W. A ratiometric Raman probe for live-cell imaging of hydrogen sulfide in mitochondria by stimulated Raman scattering. *Analyst* **143**, 4844–4848 (2018).
121. Zhang, J. et al. Small unnatural amino acid carried Raman tag for molecular imaging of genetically targeted proteins. *J. Phys. Chem. Lett.* **9**, 4679–4685 (2018).
122. Hiramatsu, K. et al. High-throughput label-free molecular fingerprinting flow cytometry. *Sci. Adv.* **5**, eaau0241 (2019).
123. Suzuki, Y. et al. Label-free chemical imaging flow cytometry by high-speed multicolor stimulated Raman scattering. *Proc. Natl Acad. Sci. USA* <https://doi.org/10.1073/pnas.1902322116> (2019).

Acknowledgements

We thank L. Wei, L. Shi, H. Xiong and X. Liu for reading the manuscript. W.M. acknowledges support from National Institutes of Health (NIH) Director's New

Innovator Award, NIH R01 (EB020892 to W. M.), NIH R01 (GM128214 to W. M.), NIH R01 (GM132860 to W. M.), the Alfred P. Sloan Foundation, the Camille and Henry Dreyfus Foundation, and a Pilot and Feasibility grant from the New York Obesity Nutrition Research Center. F.H. acknowledges support from a Raymond and Beverly Sackler Center Postdoctoral Fellowship.

Author contributions

F. H., L. S., and W. M. conceived and wrote the paper.

Competing interests

The authors declare no competing interests.

Additional information

Reprints and permissions information is available at www.nature.com/reprints.

Correspondence should be addressed to W.M.

Peer review information: Rita Strack was the primary editor on this article and managed its editorial process and peer review in collaboration with the rest of the editorial team.

Publisher's note: Springer Nature remains neutral with regard to jurisdictional claims in published maps and institutional affiliations.

© Springer Nature Limited 2019